The Influence of Specific Heat Ratio on the Flow Characteristics of Over-Expanded Single Expansion Ramp Nozzles

Zhenghe Wang[1], Tao Yu[2,3], Yunfeng Guo[2], Rui Liu[2] and Yang Yu[1,2,3,*]

[1] School of Mechanical Engineering, Zhengzhou University of Aeronautics, Zhengzhou, 450046, China

[2] Chongqing Key Laboratory of Green Aviation Energy and Power, Chongqing Jiaotong University, Chongqing, 400074, China

[3] The Green Aerotechnics Research Institute of Chongqing Jiaotong University, Chongqing, 401120, China

INFORMATION

Keywords:
Single expansion ramp nozzle
over-expansion
specific heat ratio
flow characteristic
shock wave/boundary layer interaction

DOI: 10.23967/j.rimni.2024.10.56457

SCIPEDIA Revista Internacional de Métodos Numéricos para Cálculo y Diseño en Ingeniería

Revista Internacional Métodos numéricos para cálculo y diseño en ingeniería RIMNI CIMNE

The Influence of Specific Heat Ratio on the Flow Characteristics of Over-Expanded Single Expansion Ramp Nozzles

Zhenghe Wang[1], Tao Yu[2,3], Yunfeng Guo[2], Rui Liu[2] and Yang Yu[1,2,3,*]

[1]School of Mechanical Engineering, Zhengzhou University of Aeronautics, Zhengzhou, 450046, China

[2]Chongqing Key Laboratory of Green Aviation Energy and Power, Chongqing Jiaotong University, Chongqing, 400074, China

[3]The Green Aerotechnics Research Institute of Chongqing Jiaotong University, Chongqing, 401120, China

ABSTRACT

The flow field in the over-expanded single expansion ramp nozzle (SERN) demonstrates pronounced flow separation, intricate interactions involving intersecting and reflecting shocks, and mutual interference between shocks and boundary layers. Discrepancies arising from cold flow experiments *vs.* actual operational conditions introduce a notable influence of the specific heat ratio (γ) on shock angles and shock/boundary layer interactions, thereby impacting the entire flow field. In this study, the differences between the cold flow conditions inside the nozzle and the actual operating conditions are found through numerical simulations, and the effects of γ on the shock structure and the shock/boundary layer interactions in an over-expanded SERN are investigated. Results indicated that cold flow experiments inadequately represented the authentic flow dynamics within the nozzle. Under varying nozzle pressure ratios (NPR) and γ conditions, the two-dimensional (2D) flow field structure of the over-expanded SERN exhibited diverse configurations of separated shock structures, encompassing Mach reflections, regular reflections, and triangular shock waves. Furthermore, alterations in γ influenced the movement of separation and reattachment points, induced pressure variations, and potentially triggered a transition in flow separation patterns. The changes in NPR and γ also modified the position and scale of the separation region, with an augmented NPR intensifying this effect. Moreover, the smaller values of γ were likely to lead to flow separation, separation pattern transitions, and changes in the structure of the separated shock waves. Compared with the 2D case, the three-dimensional outcomes indicated that the separated shock structure on the symmetry plane remained consistent, whereas that away from the symmetry plane contracted inward. The interaction patterns of the separated shocks on the ramp and flap also changed.

OPEN ACCESS

Received: 23/07/2024

Accepted: 07/11/2024

Published: 07/04/2025

DOI
10.23967/j.rimni.2024.10.56457

Keywords:
Single expansion ramp nozzle
over-expansion
specific heat ratio
flow characteristic
shock wave/boundary layer interaction

*Correspondence: Yang Yu (yuyang227@vip.sina.com).

Glossary/Nomenclature/Abbreviations

SERN	Single expansion ramp nozzle
γ	Specific heat ratio
NPR	Nozzle pressure ratio
SWBLI	Shock wave/boundary layer interaction

1 Introduction

The high-speed air-breathing propulsion system utilises the oxygen in the atmosphere as the oxidiser to react with the carried fuel, thereby greatly reducing the take off weight and cost of the aircraft [1,2]. The highly representative scramjet engine is considered the optimal power device for achieving hypersonic flight within the Earth's atmosphere. It does not use rotating components and can provide propulsion to the aircraft at hypersonic speeds in the atmosphere [3]. Therefore, the hypersonic, air-breathing propulsion technology, with the scramjet engine as its core, has become a key focus of research in various countries [4,5]. As the primary thrust-generating component of the scramjet engine, the nozzle also provides partial lift and pitching moment to the aircraft, making it a critical component for achieving maximum thrust in air-breathing hypersonic flight. As a type of over-expanded nozzle, the single expansion ramp nozzle (SERN) has excellent weight reduction effects and can effectively reduce the base drag and friction losses of the nozzle [6,7], making it the most ideal exhaust system currently available [8,9].

Over-expanded SERN is usually accompanied by complex phenomena such as shock waves, expansion waves and shock wave/boundary layer interaction (SWBLI) [10]. Computational fluid dynamics (CFD) is an important tool for studying dynamic flow characteristics in unsteady flow phenomena in supersonic nozzles [11]. However, the computational cost and time are high for unsteady flow simulations, and the numerical results may not accurately capture complex phenomena such as over-expanded flow separation and SWBLI. Thus, these results do not fully reflect the actual flow field and nozzle characteristics. Moreover, the results of exhaust system design obtained through numerical simulation methods often need to be validated through wind tunnel experiments [12,13]. Efficient and cost-effective wind tunnel experimental techniques, as well as methods for data processing, are crucial technologies in developing exhaust systems.

Given the limitations imposed by factors such as inlet conditions and temperature, simulating the actual operating conditions of a nozzle in ground-wind tunnel experiments may not fully capture the complex flow phenomena inside SERNs. As a result, many researchers have conducted studies on SERN based on cold flow experiments. For example, Kumar et al. [14] investigated the thrust augmentation performance of SERN through cold flow experiments. The results revealed that the flow separation on the expansion ramp and the associated downstream curved shock formed by the separation bubble lead to a thrust increment that is much lower than the predictions of the inviscid theory. Lv et al. [15] obtained the flow field characteristics, wall pressure distribution, and force information of SERN through cold flow experiments. They combined experimental data with numerical methods to study the performance of SERN under various operating conditions, thereby verifying the reliability of SERN design methods based on maximum thrust theory under geometric constraints. They also conducted cold flow experiments on the pattern transition of the turbine based combined cycle exhaust system. Additionally, they simulated the flow field of the exhaust system using numerical methods and the results were compared with experimental data. The results of the comparison indicated that although the flow field inside the exhaust system is highly complex, it is decoupled from the external flow field [16]. Mo et al. [13] proposed a novel method for optimising

the shape transition from circular to rectangular for a three-dimensional (3D) scramjet nozzle. They verified the accuracy of the proposed method through CFD simulations and cold flow experiments. Chen et al. [17] validated the effectiveness and accuracy of their proposed method for designing scramjet nozzles within a predetermined geometric space through cold-flow experiments and 3D numerical calculations.

The cold flow experiment offers the advantages of low energy consumption and direct measurement of the nozzle's mechanical performance, thereby providing certain advantages in the initial aerodynamic design of the exhaust system. However, in the cold flow experiments conducted on the exhaust system, the air is used as the operating fluid, whereas the actual operating fluid in the nozzle is post combustion exhaust gas. Given the disparity in specific heat ratio (γ) between the two fluids, differences arise in the simulated target flow field. γ affects the angles of shock waves and the results of SWBLI when extensive flow separation, accompanied by numerous intersecting shock waves and SWBLI, occurs within the nozzle.

Studies conducted under cold flow conditions cannot replicate the actual operating state of the nozzle. Therefore, researchers have begun to focus on compensation and control methods for the specific heat ratio to achieve more accurate results. Cortes et al. [18] coupled a supersonic combustion chamber test bench with a supersonic nozzle to numerically analyse the behaviour of hot and cold flows. The results showed that the parameters at the combustion chamber inlet significantly affect the flow conditions at the nozzle exit. Sung et al. [19] investigated the flow characteristics of a supersonic nozzle directly connected to the combustion chamber, taking into account the influence of specific heat ratio through numerical methods. Hirschen et al. [20] studied the performance of scramjet nozzles under different flight conditions and found that increasing the specific heat ratio reduces the pressure coefficient. Zebbiche [21] observed that the design of nozzles for hypersonic vehicles must consider variable specific heat effects and proposed a design method for axisymmetric minimum-length nozzles. Sellam et al. [22] developed an analytical model to study the influence of specific heat ratio on thrust vectoring in supersonic nozzles. Chen et al. [23] comprehensively analysed the impact of high-temperature variable specific heat on nozzle flow and proposed two methods to address the false thrust problem caused by variable specific heat effects.

Although there have been breakthroughs in nozzle optimization design and flow characteristic analysis considering the specific heat ratio, the mechanisms by which the specific heat ratio influences the nozzle flow field remain unclear, particularly in the more complex flow conditions of over-expanded states. This study aims to explore the impact of variations in the specific heat ratio of the SERN during ground-based cold flow wind tunnel experiments and practical operations, along with the influence of γ on the flow characteristics of the over-expanded SERN. In this study, the accuracy of the numerical methods used is first verified, and then the difference between the cold flow conditions and the actual operating conditions of the nozzle is investigated. The effect of γ on the shock wave structure and SWBLI in an over-expanded SERN is investigated in two- and 3D, and finally the effect of specific heat ratio on the mechanical properties of the nozzle is discussed.

2 Models and Numerical Methods

The steady, compressible two-dimensional (2D) Reynolds-averaged Navier–Stokes equations are employed as the governing equations [24,25]. A turbulence model is introduced to capture the turbulent characteristics. In this study, the Re-normalization group (RNG) theory is utilised, and the RNG k-ε model with wall functions is applied to the Navier–Stokes equations to capture certain turbulent features effectively [26,27]. The control equations are discretised using a finite volume integration

scheme. In this method, the computational domain is divided into discrete volume cells, and integral calculations are performed on each cell, enabling the solution of the governing equations within the discretised framework. During the computations, the dynamic viscosity coefficient is calculated using the Sutherland formula, and the Roe second-order upwind scheme is employed for the discretisation of the convective terms. The method based on Green–Gauss cells is employed for gradient calculations. This method estimates the variable gradients through interpolation from neighbouring cells.

Fig. 1a shows the SERN model. The model employs a straight wall design with an expansion angle of 25° on the ramp, a nozzle design with a nozzle pressure ratio (NPR) of 20, and an area expansion ratio of 2.896. The flap length is the same as the ramp length. The boundary conditions are set to match the experimental conditions, with an NPR of 3.0. The numerical simulation grids are shown in Fig. 1b and c. The boundary conditions employed in the numerical computation are consistent with those described in the literature [28]. The nozzle's NPR is 3.0. At the inlet, the total pressure is set to 93,243.66 Pa with a static temperature of 300 K; under far-field pressure conditions, the Mach number is 0, with a pressure of 31,073.02 Pa and a static temperature of 300 K; the outlet pressure is set to 31,073.02 Pa with a static temperature of 300 K. The wall boundary conditions are specified as a no-slip condition. Moreover, the mesh is refined, particularly in the regions close to the walls, to ensure that the $y+$ values in these regions are between 30 and 60, satisfying the requirements of the wall function. The residual values are monitored throughout the numerical simulation. The convergence criterion is considered to have been reached when the residual value drops to one thousandth of the relative initial value, which usually requires approximately 20,000 iterations.

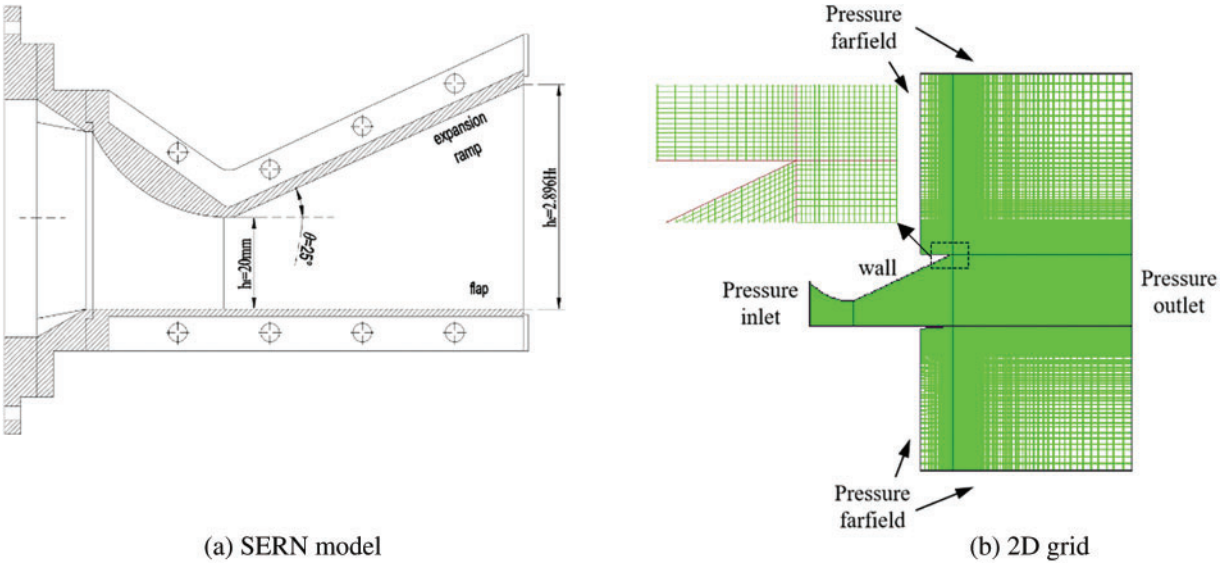

(a) SERN model (b) 2D grid

Figure 1: (Continued)

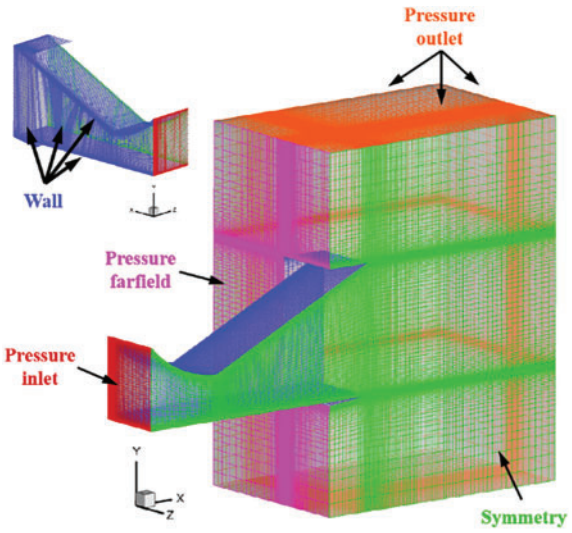

Figure 1: SERN model and grid

Fig. 2a and b compares the pressure distribution on the ramp and flap of the nozzle obtained from numerical simulations using three sets of grids with different qualities in the 2D and 3D models. The above-mentioned grid is defined as a medium grid, the grid with doubled grid nodes in the x and y directions is defined as a fine grid, and the grid with halved grid nodes in the x and y directions is defined as a coarse grid. The different grid resolutions are shown in Table 1. Fig. 2a and b shows that the separation points on the ramp and flap vary slightly with the change in grid density. However, the pressure distributions on the ramp and flap are nearly identical, with deviations between them all being less than 3%. These deviations fall within an acceptable range, indicating that satisfactory computational accuracy can be achieved using the medium grid. Additionally, Fig. 2c provides a comparison between the results obtained from the full 3D model and the half model. The results obtained from both models are in good agreement, thereby justifying the use of the half model for the 3D numerical calculations.

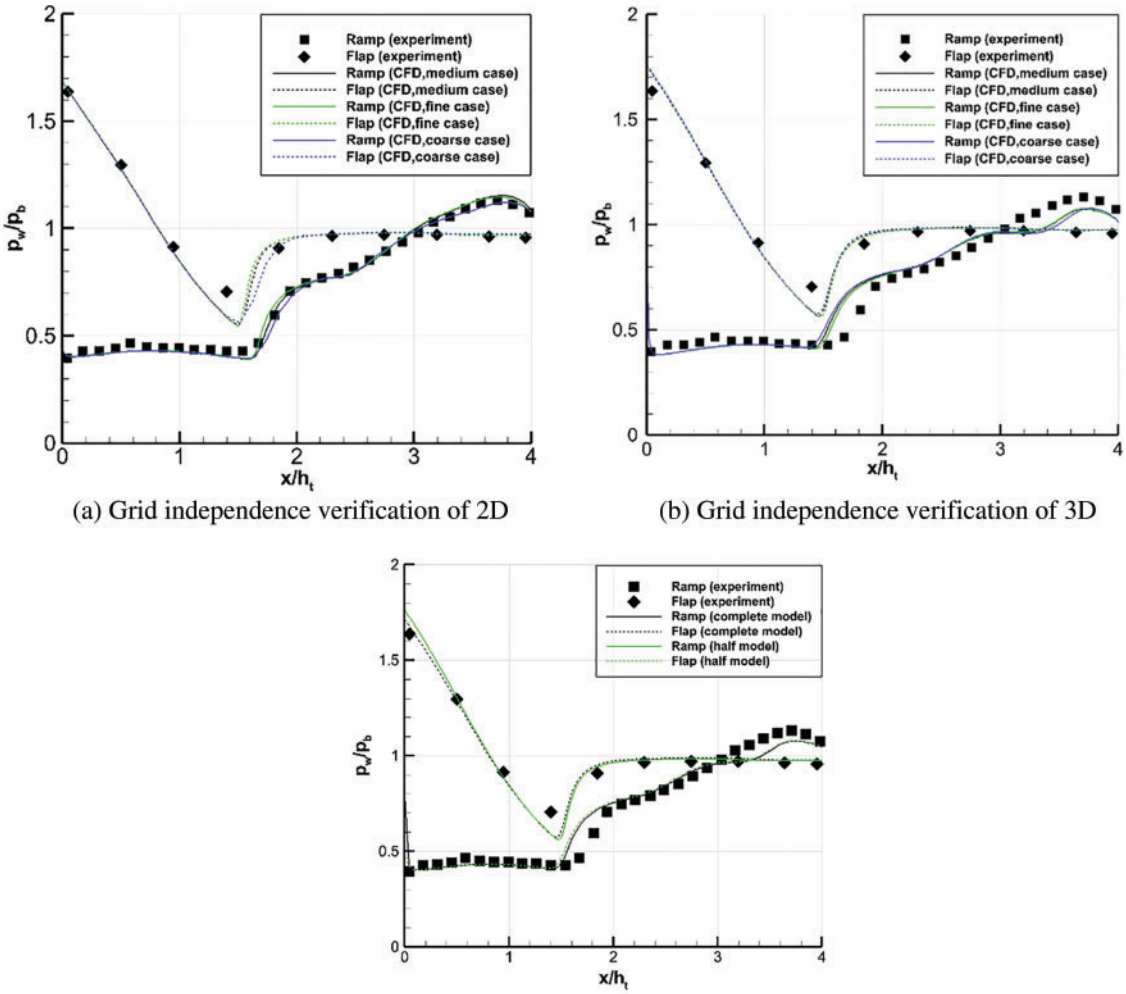

(a) Grid independence verification of 2D

(b) Grid independence verification of 3D

(c) Comparative verification of 3D full model and half model

Figure 2: Grid independence verification and 3D full/half model comparison verification

Table 1: Different grid resolutions

	Coarse	Medium	Fine
2D	42,358	146,894	556,842
3D	637,692	1,187,324	4,322,658

3 Result and Discussion

3.1 Comparison of Cold Flow Conditions with Actual Operating Conditions

This section provides a numerical simulation of the actual operating condition of SERN, and its results are compared with those of cold flow experiments and numerical simulations. The gas composition and temperature at the inlet conditions of the actual operating conditions numerical

simulation are consistent with the results obtained by Cutler et al. [29] at the outlet of a scramjet combustor. The inlet temperature of SERN is 1676 K, and the gas composition is shown in Table 2. The remaining boundary conditions are the same as those used in the cold flow numerical simulation.

Table 2: Inlet air composition

Chemical formula	N_2	O_2	H_2O	CO	CO_2	C_2H_4
Mole fraction	0.800	0.110	0.039	0.010	0.033	0.008

Fig. 3 shows the wall pressure distribution of the SERN in cold flow experiments, cold flow numerical simulations, and actual operating conditions. Under the two NPRs of 2.6 and 3.0, remarkable differences are observed in the pressure distribution on the ramp and flap of the SERN between cold flow experiments and actual operating conditions. In actual operating conditions, the pressure distribution is high, and the separation point is close to the nozzle outlet.

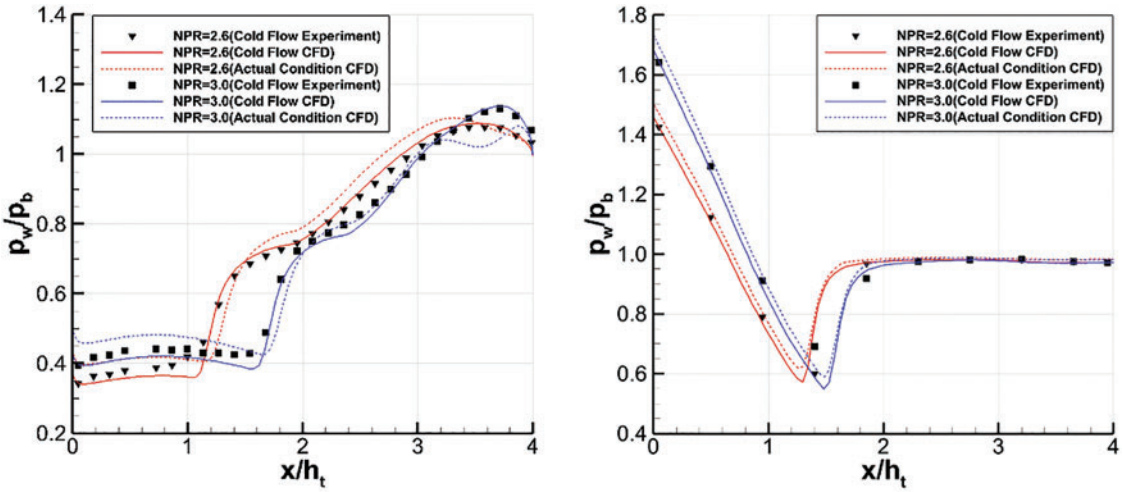

(a) Pressure distribution on ramp (b) Pressure distribution on flap

Figure 3: Comparison of the wall pressure distribution between cold flow experiment, cold flow numerical calculation and actual operating condition numerical calculation

The observed phenomenon can be attributed to different Ma distributions within the SERN because of varying γ values under the same NPR conditions. According to Eq. (1), the inlet and outlet area ratio is constant; thus, changing γ causes variations in Ma. For instance, in the cold flow experiment with γ equal to 1.40, high Ma is achieved internally within the SERN; however, under actual operating conditions, the gas γ is relatively small, resulting in low Ma. The relationship between Ma and static pressure can be derived from Eq. (2). Thus, different Ma distributions lead to distinct static pressure distributions on the SERN wall. According to Eq. (2), the static pressure is inversely proportional to γ. This finding indicates that an increase in γ results in a decrease in static pressure within the SERN, whereas a decrease in γ leads to an increase in static pressure.

$$\left(\frac{A}{A^*}\right)^2 = \frac{1}{Ma^2}\left[\frac{2}{\gamma+1}\left(1+\frac{\gamma-1}{2}Ma^2\right)\right]^{\frac{(\gamma+1)}{(\gamma-1)}} \tag{1}$$

$$\frac{p_{st}}{p_0} = \left(1 + \frac{\gamma - 1}{2} Ma^2\right)^{\frac{\gamma}{\gamma - 1}} \tag{2}$$

where A is the local cross-sectional area, A^* is the throat cross-sectional area, p_{st} is the static pressure and p_0 is the total pressure.

Lift (L), axial thrust (F_x) and pitching moment (M_z) are introduced to assess the performance parameters of SERN; they reflect the mechanical characteristics of the nozzle [30]. In this study, thrust (F) is obtained by integrating the relative pressure over the surface of the nozzle. The x-component of F is F_x, and the y-component is L, referred to as F_y. The centre of the nozzle throat is the reference point for the M_z. These parameters are defined as follows:

$$F = \int (p_w - p_b)\, ds \tag{3}$$

$$F_x = \int (p_w - p_b)\, dy \tag{4}$$

$$L = F_y = \int (p_w - p_b)\, dx \tag{5}$$

The pressure distribution on the wall directly determines the performance of the SERN. However, the aforementioned analysis indicates that variations in γ result in different static pressure levels inside the SERN, thereby causing mechanical performance differences between cold flow conditions and actual operating conditions. Table 3 presents the mechanical performance data of the SERN under actual operating conditions and cold flow experiments at NPR values of 2.6 and 3.0. The data demonstrates that accurate measurement of the SERN's mechanical performance cannot be achieved under cold flow conditions in the over-expanded state.

Table 3: Mechanical performance of SERN under actual operating conditions and cold flow conditions

	NPR	F_x (N)	L (N)	M_z (Nm)
Actual operating cond-tions	2.6	−1018.3	−642.7	50.7
	3.0	−815.6	−759.3	42.1
Cold flow conditions	2.6	−989.9	−660.4	49.7
	3.0	−808.2	−731.7	43.9

In summary, the flow characteristics and mechanical performance of a SERN under cold flow conditions significantly differ from those under the actual operating conditions, with γ being the primary factor influencing such differences. The following sections discuss the topic from the 2D and 3D perspectives to investigate further the influence of γ on the flow characteristics of over-expanded SERN. Moreover, the effects of γ on shock wave structures and SWBLI within the flow field are analysed.

3.2 The Effect of Specific Heat Ratio on the 2D Flow Field of Over-Expanded SERN

Given that the γ of actual combustion gases is typically lower than that of air, we have chosen γ values of 1.25, 1.30, 1.35, and 1.40 for this study. Additionally, we recognize that under conditions of

over-expansion in the nozzle, the NPR is usually relatively low; therefore, we have selected NPR values of 3.0, 3.5, and 4.0.

Fig. 4 shows the flow field structure inside the SERN under different NPR and γ conditions. When the NPR is 3.0 and γ is 1.40, the flow experiences an expansion wave as it passes through the throat. This scenario results in significantly lower wall pressure than the ambient pressure, thereby creating an adverse pressure gradient. This adverse pressure gradient induces boundary layer instability, leading to the separation of the flow on the ramp and flap and the formation of a shock wave structure known as Mach reflection. As γ decreases gradually, the length of the separation shock wave on the ramp shows minimal change, whereas the length of the separation shock wave on the flap noticeably increases. Additionally, the Mach stem moves upstream and shortens, causing the entire separation shock wave structure to move near the nozzle outlet. When the NPR is 3.5 and γ is 1.40, the separation shock waves on the ramp and flap intersect, thereby forming a Mach reflection structure. As γ decreases, the Mach stem gradually shortens and eventually disappears, resulting in the transition from Mach reflection to regular reflection. When the NPR is 4.0, the entire separation shock wave structure exhibits regular reflection. The extent of the backward movement of the separation shock wave structure diminishes, with the decrease in γ. However, remarkable changes occur within the structure. For instance, when γ is 1.30, a short shock wave forms after the intersection point of the separation shock waves. Moreover, the reflected shock wave connecting the two separation shock waves forms a structure similar to a triangular shock wave. The short wave connecting the reflected shock waves moves towards the nozzle outlet and gradually grows in length by further reducing γ to 1.25.

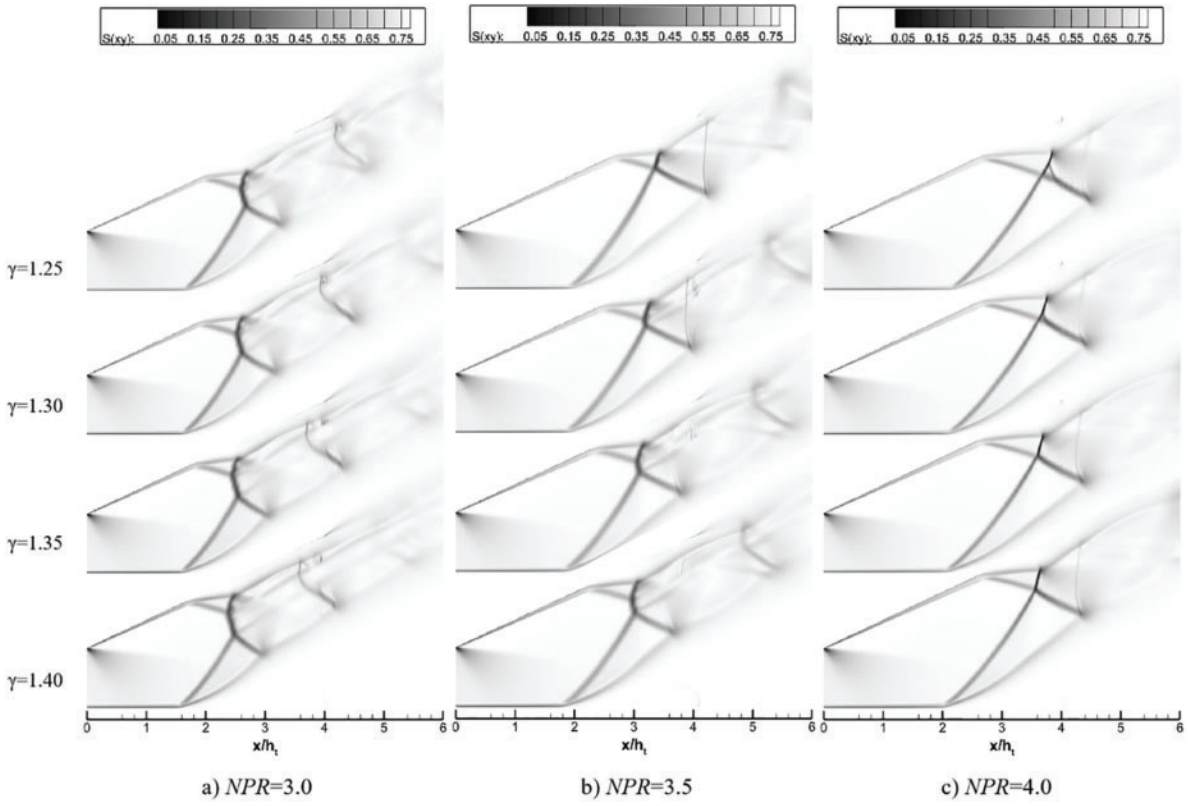

Figure 4: Flow field structure in SERN under different NPR and γ conditions

Fig. 5 shows the wall pressure distribution and shear stress distribution of SERN under different NPR and γ conditions. After a stable wall pressure regime, a sudden pressure jump caused by the occurrence of separation shock waves can be observed. These separation shock waves also induce flow boundary separation, leading to the formation of large separation bubbles, which are evident in the shear stress distribution along the wall. Decreasing γ increases the static pressure within the SERN. This increase is reflected in the pressure distribution along the ramp. Moreover, the separation and reattachment points shift downstream, accompanied by certain changes in pressure. This phenomenon alters the shape of the separation region. The degree of the backward movement of the separation and reattachment points, as well as the pressure variations influenced by γ, differs under different NPR conditions. The flow does not reattach to the ramp when γ is 1.40 and the NPR is 4.0. For reduced γ values, all shear stress distribution curves intersect with $\tau_x = 0$ for a second time, indicating the reattachment of the flow on the ramp. This finding suggests that the wake flow of the SERN undergoes oscillation near the ramp trailing edge, transitioning from the RSS (ramp) pattern to the FSS pattern. In summary, under different NPR conditions, varying γ has a series of effects on the wall pressure distribution and shear stress distribution of SERN, including the movement of separation and reattachment points, pressure changes, and the transition of flow separation patterns.

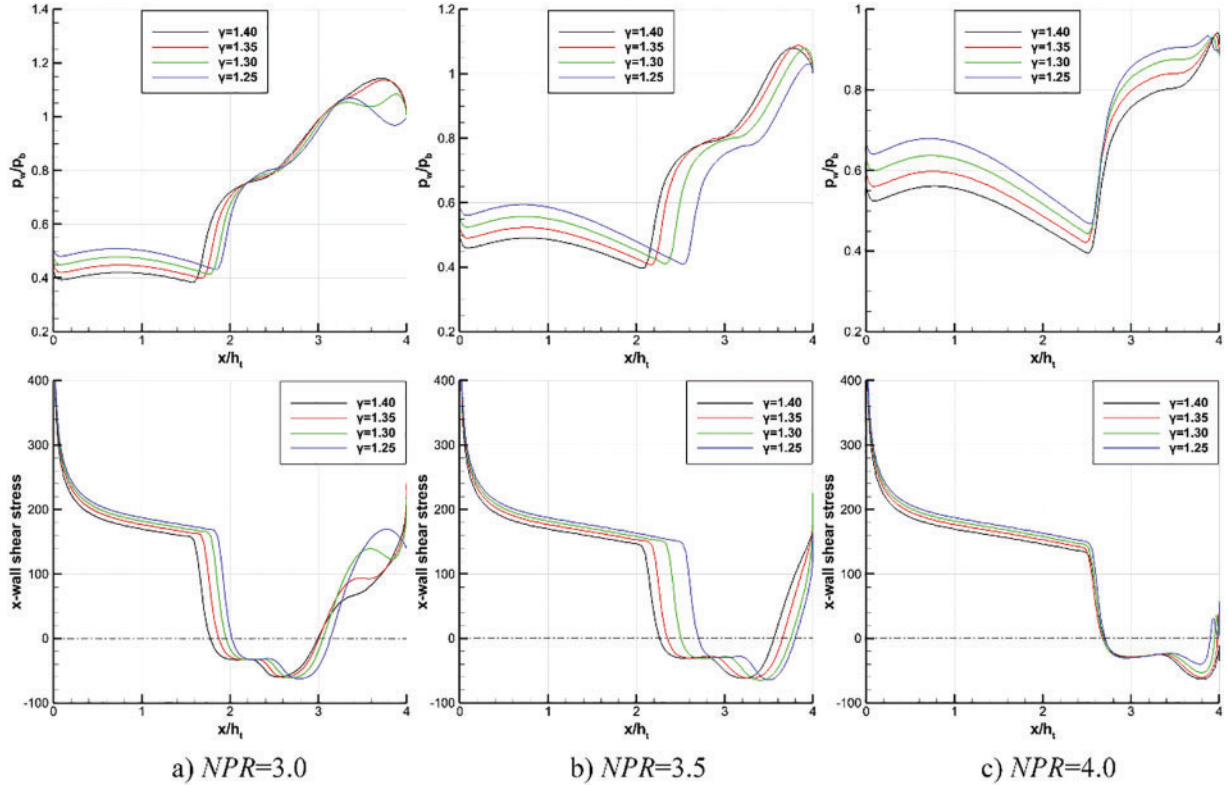

Figure 5: Wall pressure distribution and shear stress distribution of SERN under different NPR and γ conditions

Fig. 6 demonstrates the trend of the dimensionless thrust, lift and pitching moment of the nozzle at different NPR and γ operating conditions. All parameters are benchmarked against the nozzle performance at γ of 1.40. The reference point of the pitching moment is set as the midpoint of the nozzle throat. The changes in thrust and lift are relatively stable when γ decreases, whereas the changes

in pitching moment are obvious. When γ decreases from 1.40 to 1.25, the thrust decreases by 0.34%, the lift increases by 6.26%, and the pitching moment decreases by 26.2% at an NPR of 3.0. At NPRs of 3.5 and 4.0, the thrust varies considerably across NPR conditions, thereby decreasing by 2.87% and increasing by 15.8%. Lift force also varies in different NPR conditions, as it shows an increase of 9.84% and a decrease of 13.96%. The pitching moment has a large variation; it decreases by 149.4% and 184.9%, indicating that the variation of γ has a minimal effect on the thrust and lift, but a considerable effect on the pitching moment.

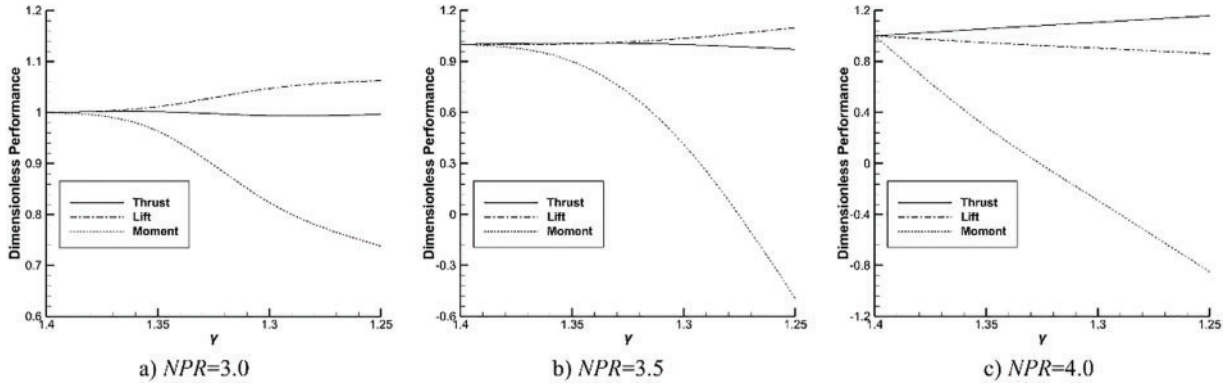

Figure 6: Dimensionless mechanical properties of SERN for different NPR and γ working conditions

Fig. 7 shows the effects of SWBLI in a separated flow field when NPR is 3.0 and γ is 1.40. Fig. 7a presents the velocity contour map of the local flow field on the ramp, whereas Fig. 7b depicts the distribution of shear stress on the ramp. The starting point (X_{ini}) and separation point (X_{sep}) of SWBLI are used to describe the extent of the influence of the separated shock wave. The location of the incident point (X_{inc}) of the reflected shock wave corresponds to the maximum height of the separation bubble and is used to assess the degree of flow separation. Additionally, the position of the reattachment point (X_{att}) is a crucial parameter during the process of flow reattachment.

Table 4 provides nondimensionalised data on the location and scale of the separated SWBLI for different NPR and γ values. These data serve as crucial parameters for evaluating the extent of flow separation and the influence of SWBLI on the flow field. The table shows that varying the NPR and γ values affects the position and scale of the SWBLI separation region. Under the same NPR conditions, a decrease in γ causes X_{ini}, X_{sep}, X_{sep}, and X_{sep} to move towards the vicinity of the nozzle trailing edge. This finding indicates that the separation region shifts towards the downstream direction as γ decreases. The length of the separation region (L_{sep}) and the maximum height of the separation bubble exhibit changes that do not follow a consistent pattern. This outcome may be attributed to variations in the structure of the separation shock wave. Thus, the influence of γ on the flow field is not singular and likely involves complex physical mechanisms. Furthermore, different NPR values affect the position and scale of the separation region. As NPR increases, the separation region shifts downstream, and the length of the separation region increases. This finding indicates the clear influence of NPR on the position and scale of the SWBLI separation region, with its impact gradually strengthening. In summary, the table demonstrates that the position and scale of the SWBLI separation region are influenced by parameters such as γ and NPR. Changes in these parameters alter the position and scale of the separation region, thereby impacting the extent of flow separation and SWBLI in the flow field.

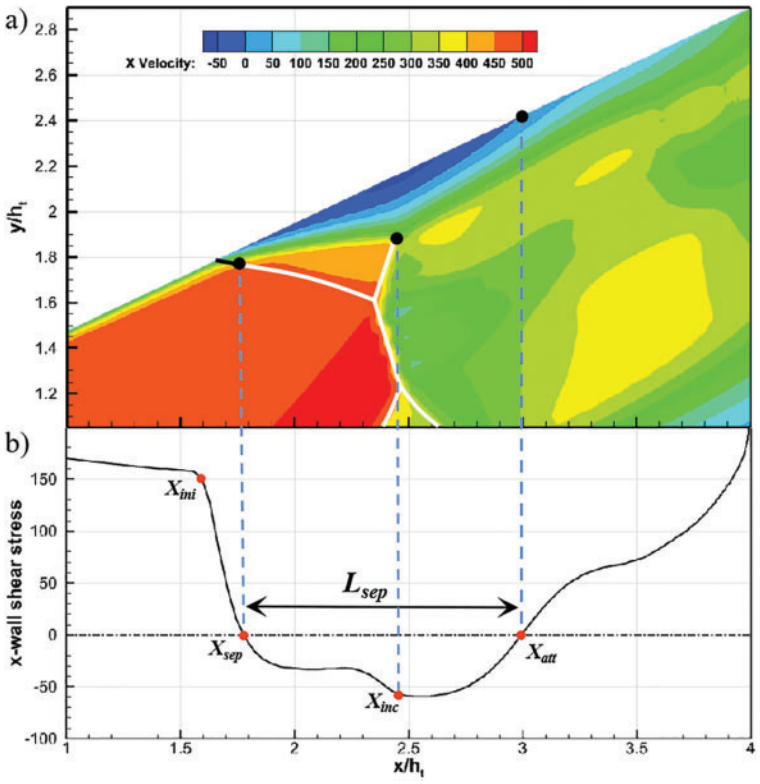

Figure 7: Flow field structure and shear stress distribution of the local SWBLI on the ramp

Table 4: Scale changes in the separation zone under different NPR and γ conditions

NPR	γ	X_{ini}	X_{sep}	X_{inc}	X_{att}	L_{sep}	Maximum height of separation bubble
3.0	1.25	1.862	2.019	2.694	3.136	1.117	0.144
	1.30	1.784	1.955	2.616	3.054	1.099	0.140
	1.35	1.706	1.872	2.534	3.007	1.135	0.140
	1.40	1.592	1.777	2.439	2.995	1.218	0.143
3.5	1.25	2.522	2.701	3.443	3.799	1.098	0.156
	1.30	2.334	2.507	3.257	3.747	1.240	0.172
	1.35	2.178	2.354	3.157	3.652	1.271	0.171
	1.40	2.059	2.261	3.033	3.556	1.295	0.143
4.0	1.25	2.558	2.705	3.834	3.981	1.276	0.284
	1.30	2.522	2.698	3.748	3.946	1.248	0.257
	1.35	2.484	2.687	3.680	3.897	1.210	0.234
	1.40	2.521	2.678	3.633	/	/	0.210

Fig. 8 demonstrates the changes in wall separation point position and separation pressure during the SERN start up process. x_{sep}(ramp) and p_{sep}(ramp) are the separation point position and pressure of the ramp, and x_{sep}(flap) and p_{sep}(flap) are the separation point position and pressure of the flap. Under different γ conditions, the variation rule of the wall separation point position is almost the same. The separation pattern transition and the change in separation shock wave structure in the nozzle greatly influence the separation point position when the NPR increases. As shown in Fig. 8a and b, region 1 marks the separation pattern transition from the RSS (flap) pattern to the RSS (ramp) pattern. During this process, the position of the separation point on the flap increases dramatically, whereas the position of the separation point on the flap decreases significantly. Region 2 represents the process of transformation of the separation shock wave structure from Mach reflection to regular reflection. In this stage, the ramp separation point position decreases, whereas the flap is almost unaffected. During the start up process, the working conditions with small γ values are prone to the phenomena of flow separation, separation pattern transition, and separation shock wave structure change. Moreover, the small γ value of the working condition has high separation pressure, as shown in Fig. 8c and d. This finding implies that small γ values may lead to high separation pressures during start up, further affecting the flow characteristics.

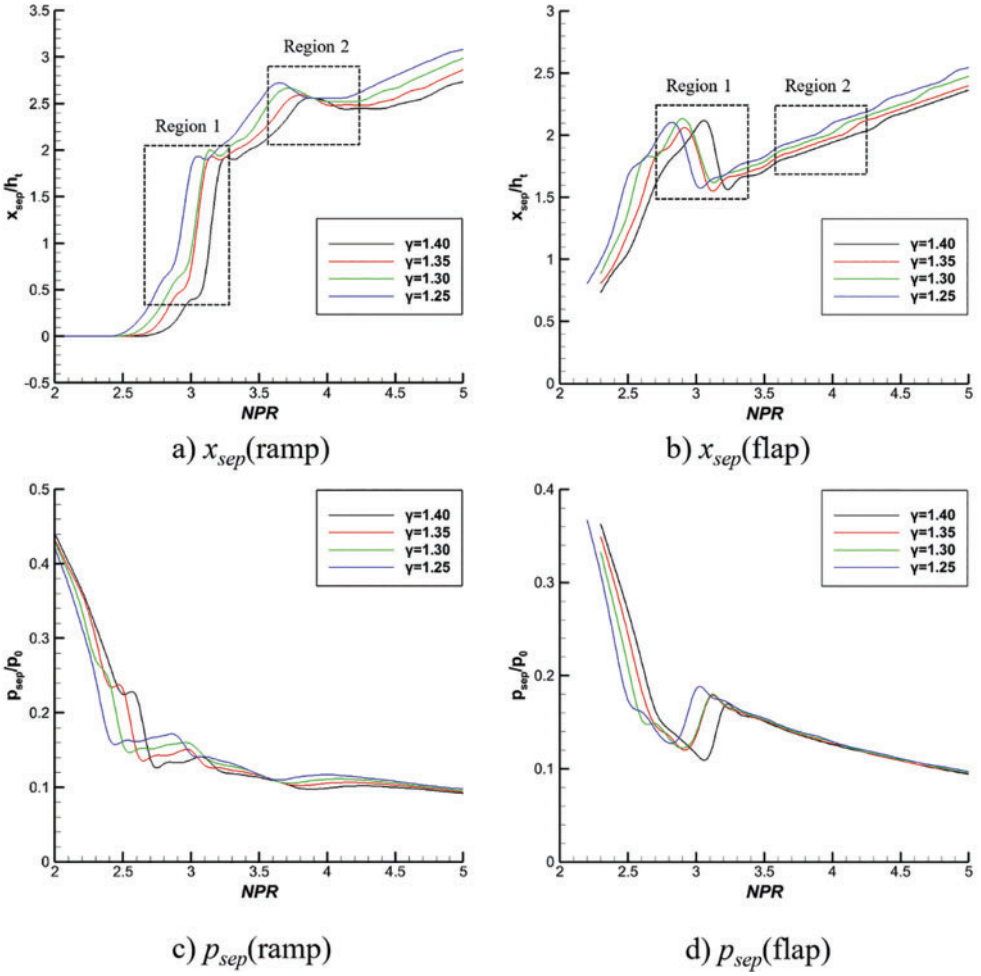

Figure 8: Position of the separation point on the nozzle wall during start up and change in separation pressure

Fig. 9 illustrates the variation of wall separation point location and separation pressure during the SERN shutdown process. Similar to the start up process, the small γ-value case exhibits a large separation point position and separation pressure during the shutdown process. As shown in Fig. 9a and b, no separation pattern transition, i.e., no RSS (ramp) pattern to RSS (flap) pattern, occurs in this section of the NPR range during the shutdown process because of the hysteresis effect. Region 1 represents the transformation of the separated shock wave structure from regular reflection to Mach reflection. During this process, the position of the separation point on the ramp surface increases, whereas the flap surface is unaffected.

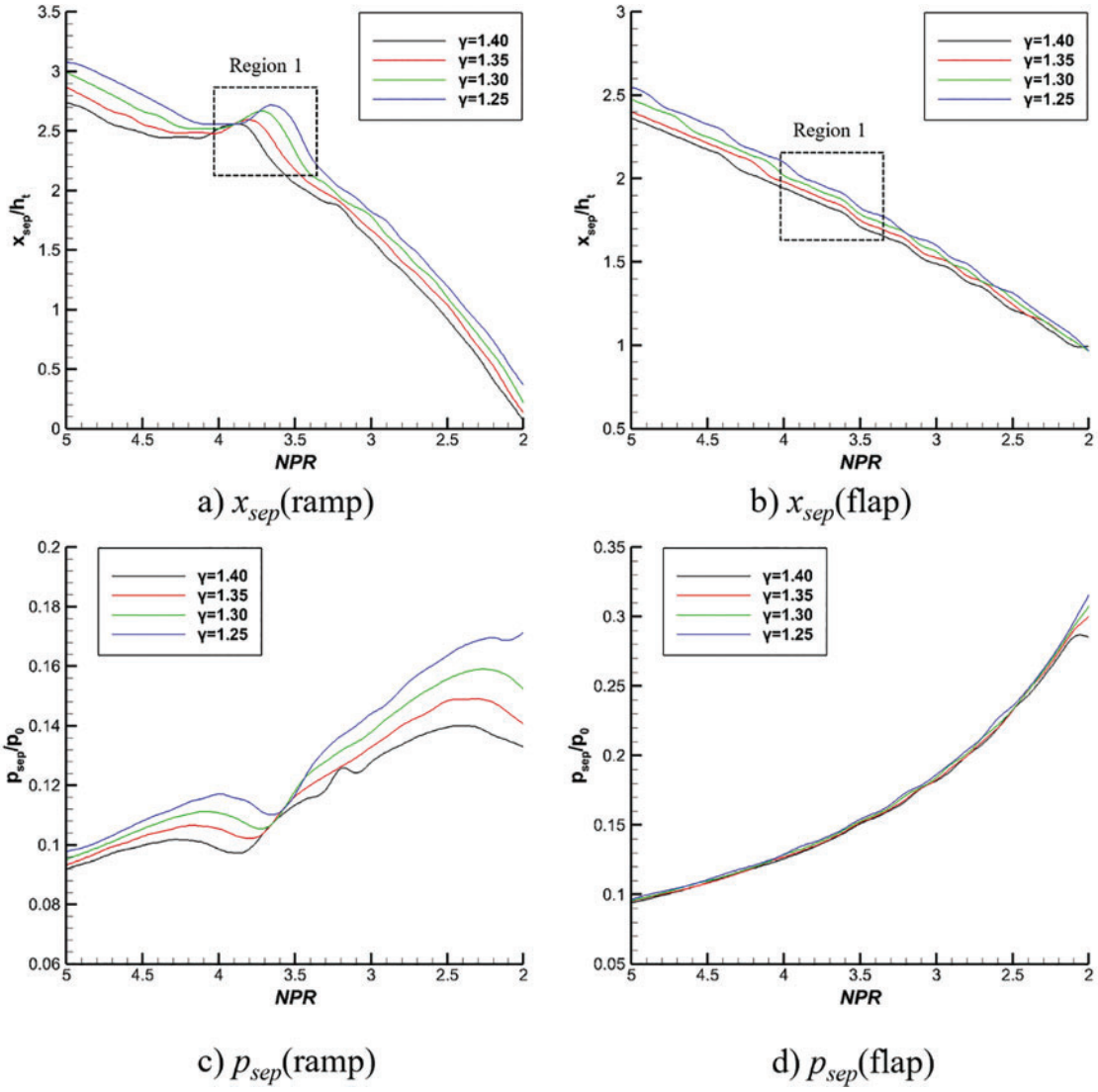

Figure 9: Position of the separation point on the nozzle wall during shutdown and change in separation pressure

3.3 The Effect of Specific Heat Ratio on the 3D Flow Field of Over-Expanded SERN

This section is based on 3D models to investigate the influence of γ on the over-expanded SERN flow field and further analyse its impact on the 3D separated shock wave structure. The 2D analysis results show that γ has a similar effect on the SERN flow field under different NPR conditions. Therefore, the focus of this section is on the NPR = 3.5 case because, under this condition, the influence of γ leads to more complex variations in the flow field.

As shown in Fig. 10, the expansion section of SERN is subjected to slice analysis to gain a deep understanding of the structure of the 3D separated flow field. The slices are taken in two dimensions, parallel to the *xy* plane and *yz* plane, and different positions are selected for observation. In particular, the slice positions parallel to the *xy* plane are $z/h_t = 0$, $z/h_t = 0.4$, $z/h_t = 0.8$, and $z/h_t = 1.2$, whereas the slice positions parallel to the *yz* plane are $x/h_t = 2.6$, $x/h_t = 2.8$, $x/h_t = 3.0$, and $x/h_t = 3.2$.

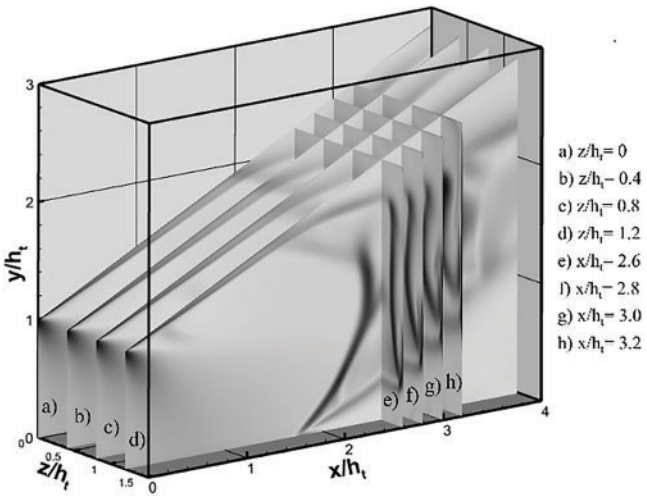

Figure 10: Slices at different positions of SERN expansion section

Fig. 11 shows the numerical Schlieren flow fields obtained from different γ conditions for slices at various positions parallel to the *xy* plane within the expansion section of the SERN. Compared with the 2D flow field, the separation shock structure in the 3D model resembles the 2D separation shock structure most closely at the symmetry plane, i.e, at $z/h_t = 0$. However, the separation shock structure contracts inwards as the slice position moves away from the symmetry plane towards the side wall. Moreover, the interaction morphology of the separation shocks on the ramp and flap changes. At the slice position of $z/h_t = 0.8$, the location of the separation point shifts towards the throat region, and the Mach stem at the intersection of the separation shocks on the ramp and flap disappears, with the weakening of the strength of the ramp separation shock. At the slice position of $z/h_t = 1.2$, the separation point continues to move towards the throat region. In addition to the separation shock on the flap intersecting with the separation shock on the flap that forms a bow-shaped shock structure, another shock separates and acts on the boundary layer above the jet, with no observed reflected shock. This finding indicates that in the 3D model, the locations where the flow separation first occurs on the ramp and flap are close to the side wall. In particular, the flow separation occurs first in the corner region. Flow separation also occurs on the side wall, and these separation shocks continue to develop and eventually converge at the symmetry plane.

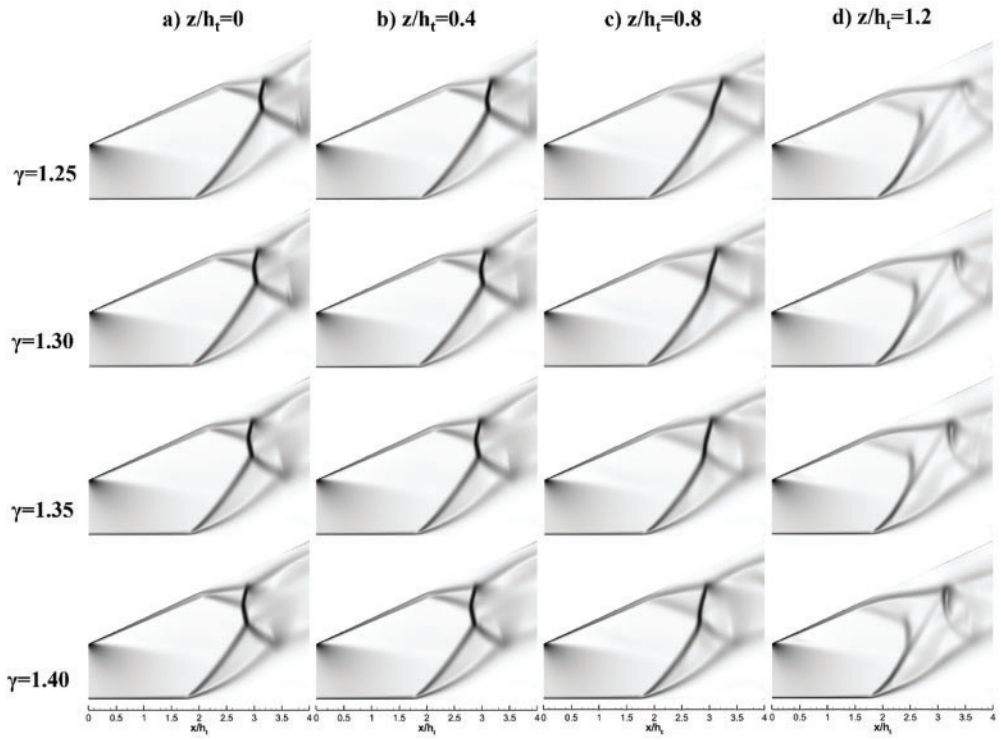

Figure 11: Numerical schlieren flow field of slices parallel to xy plane at different positions in the SERN expansion section under different γ conditions

For the numerical schlieren slice parallel to the xy plane, the variation pattern of the separated shock structures is similar to the 2D results under different γ conditions. As γ decreases, the length of the separated shock on the flap noticeably increases, the shock angle changes, and the Mach stem gradually shortens. These scenarios cause the entire separated shock structure to move towards the vicinity of the nozzle's trailing edge. However, unlike the 2D results, the 3D model shows that when NPR is 3.5, the separated shock structure does not transition from Mach reflection to regular reflection after the variation in γ, indicating the influence of 3D effects.

Fig. 12 shows the numerical Schlieren flow fields obtained by slicing the SERN expansion section at different positions parallel to the yz plane under various γ conditions. In the case of $\gamma = 1.40$, the jet boundary layers near the separation point closely adhere to the ramp and flap when the slice is positioned at $x/h_t = 2.6$. As the slice approaches the side wall, the upper and lower boundary layers gradually thicken and experience boundary layer separation. Moreover, the separation shock waves on the ramp bend downwards and connect with the separation shock waves on the flap. When the slice is positioned at $x/h_t = 2.8$, the separation shock waves on the ramp and flap exhibit an elliptical shape. Separation also occurs on the side wall. Similarly, separation is observed on the side wall when the slice is positioned at $x/h_t = 3.0$. After the intersection of separation shock waves, the dominant waves within the slice are predominantly reflected shock waves. When the slice is positioned at $x/h_t = 3.2$, the flow reattaches to the side wall, thereby forming a separation bubble. Examining the flow field structures at different slice positions under varying γ conditions reveals changes in the flow field structures at the same location as γ decreases. The reason is that the entire separation shock wave structure shifts outwards with the decrease in γ, resulting in changes in the flow field structure at the same location.

These findings align with the analysis of 2D flow fields, indicating that the influence of γ is universal and not limited to 2D flow fields.

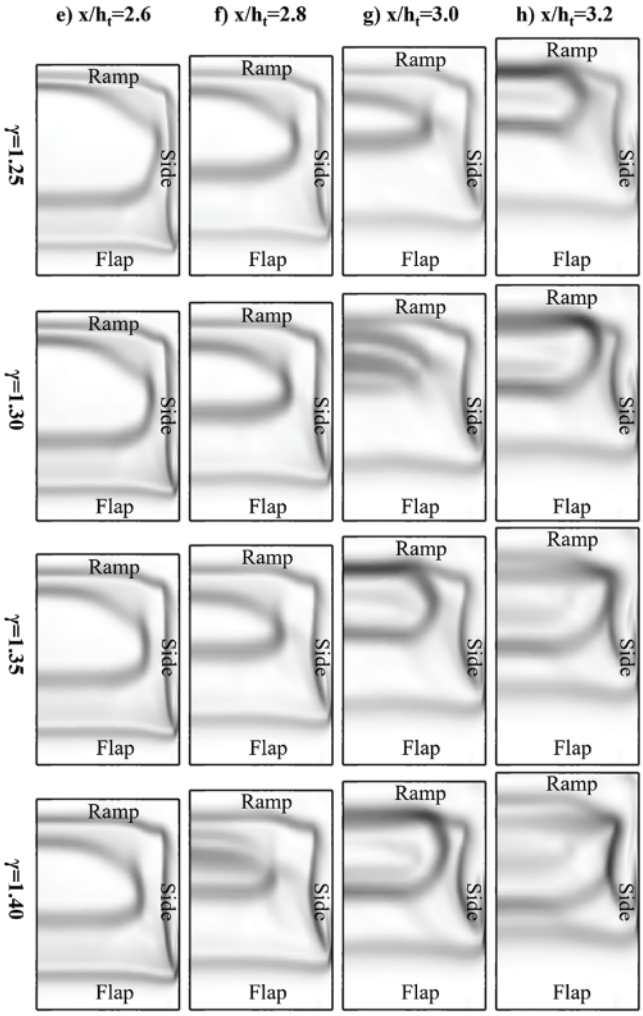

Figure 12: Numerical schlieren flow field of the slices at different positions parallel to the yz plane in the SERN expansion section under different γ conditions

Fig. 13 demonstrates the trends of the dimensionless thrust, lift and pitching moments of the nozzle under different γ operating conditions. In the 3D model, the reference point of the pitching moment is set as the midpoint of the throat at the symmetry plane of the nozzle. As γ decreases, the thrust, lift and pitching moments show a trend of decreasing and then increasing. When γ decreases from 1.40 to 1.25, the thrust decreases by 0.91%, the lift increases by 0.71%, and the pitching moment increases by 3.68%. The effects on thrust, lift, and pitching moment in the 3D model differ from those in the 2D model because of the additional degrees of freedom and complex aerodynamic effects.

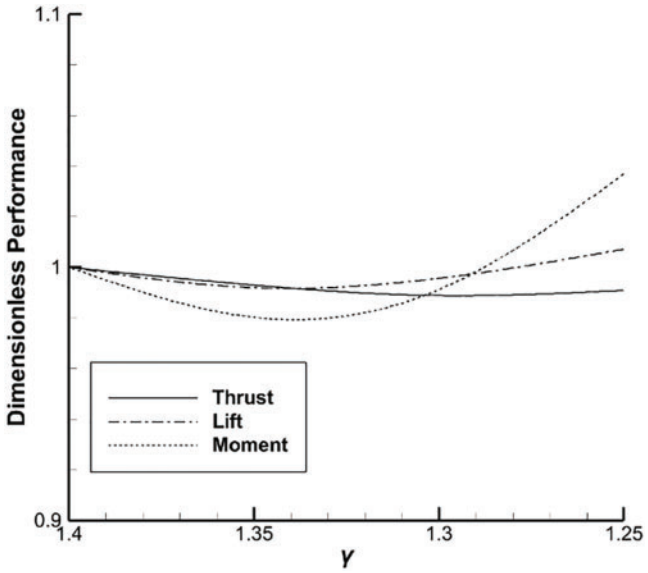

Figure 13: Dimensionless mechanical properties of SERN for different working conditions of γ

4 Conclusions

This study investigates the differences between nozzle performance under cold flow conditions and actual operating conditions. The influence of γ on the shock structure and SWBLI in the over-expanded SERNs from the 2D and 3D perspectives is also examined. The following conclusions can be drawn from this research.

Specific heat ratios alter the static pressure within the nozzle. This phenomenon results in changes in wall pressure distribution and prevents the accurate measurement of the mechanical performance of the SERN in the cold flow experiment.

Under different NPR and γ conditions, the 2D flow structure in a SERN exhibits various patterns of shock wave separation, such as Mach reflection, regular reflection, and triangular shock wave. Additionally, the wall pressure distribution and shear stress distribution are influenced by the variation of γ, including the movement of separation and reattachment points, changes in pressure, and transitions in flow separation patterns.

The complex variation of shear stress induced by SWBLI is influenced by different values of NPR and γ, which alter the location and scale of the separation region. Moreover, an increase in NPR enhances its impact.

Cases with small values of γ are prone to inducing flow separation, transition of separation modes, and variations in separation shock structures. Thus, large separation point locations and separation pressures can be observed during the start up and shutdown phases.

In a 3D flow field, the separation shock structure, located away from the symmetry plane, contracts inwards, whereas the interaction pattern between the ramp and flap separation shocks undergoes changes. Under different γ conditions, it exhibits similar variations in the separation shock structure as observed in a 2D flow field. However, the flow field structure is also influenced by 3D effects. In the future work, we will further explore effective correction methods. These correction

methods can correct the flow field deviation caused by γ by adjusting the experimental parameters or applying the correction model.

Acknowledgement: Not applicable.

Funding Statement: This work is supported by the Scientific and Technological Research Program of Chongqing Municipal Education Commission (Grant No. KJZD-M202100702), the China Space Foundation Aerospace Propulsion Public Welfare Special Fund (Grant No. KDJJ20230201006), the National Natural Science Foundation of China (Grant No. 11802124), the Special Project for Enhancing Discipline Basic Innovation Capability of ZUA (Grant No. XKZX24055).

Author Contributions: The authors confirm contribution to the paper as follows: study conception and design: Zhenghe Wang, Tao Yu, Yang Yu; data collection: Yunfeng Guo, Rui Liu; analysis and interpretation of results: Zhenghe Wang, Tao Yu, Yang Yu; draft manuscript preparation: Zhenghe Wang, Tao Yu. All authors reviewed the results and approved the final version of the manuscript.

Availability of Data and Materials: Data available on request from the authors. The data that support the findings of this study are available from the corresponding author, Yang Yu, upon reasonable request.

Ethics Approval: Not applicable.

Conflicts of Interest: The authors declare no conflicts of interest to report regarding the present study.

References

1. Baidya R, Pesyridis A, Cooper M. Ramjet nozzle analysis for transport aircraft configuration for sustained hypersonic flight. Appl Sci. 2018;8(4):574. doi:10.3390/app8040574.
2. Lv Z, Xu J, Song G, Li R, Ge J. Review on the aerodynamic issues of the exhaust system for scramjet and turbine based combined cycle engine. Prog Aerosp Sci. 2023 Nov;143(1):100956. doi:10.1016/j.paerosci.2023.100956.
3. Vanyai T, Brieschenk S, Bricalli M, Sopek T, McIntyre TJ. Thermal compression effects within a fundamental, hydrogen-fuelled scramjet. Aerosp Sci Technol. 2021 Mar;110(1):106499. doi:10.1016/j.ast.2021.106499.
4. Araújo PPB, Pereira MVS, Marinho GS, Martos JFA, Toro PGP. Optimization of scramjet inlet based on temperature and Mach number of supersonic combustion. Aerosp Sci Technol. 2021 Sep;116(2):106864. doi:10.1016/j.ast.2021.106864.
5. Li C, Xia Z, Ma L, Zhao X, Chen B, Feng Y, et al. Experimental investigation on the ignition delay of fuel-rich mixture in solid rocket scramjet. Acta Astronaut. 2022 Jan;190:112–7. doi:10.1016/j.actaastro.2021.10.001.
6. Yu T, Wu X, Yu Y, Li R, Zhang H. Establishment and validation of a relationship model between nozzle experiments and CFD results based on convolutional neural network. Aerosp Sci Technol. 2023 Oct;142:108694. doi:10.1016/j.ast.2023.108694.
7. Zhou L, Wang Z. Numerical investigation on the three-dimensional flowfield in the single expansion ramp nozzle with passive cavity flow control. J Appl Fluid Mech. 2019 Jul;12(4):1115–26. doi:10.29252/jafm.12.04.29320.
8. Inturi D, Pinnam L, Vegesna R. Effect of free boundary on the performance of single expansion nozzle. Int J Turbo Jet-Engines. 2023 May;41(2):253–265. doi:10.1515/tjj-2023-0034.

9. Nafis BM, Paul T, Hasan ABMT. Effect of flap temperature on single expansion ramp nozzle performance. AIP Conf Proc. 2017;1851:020108. doi:10.1063/1.4984737.
10. Lv Z, Xu J, Song G. Design and performance analysis of an exhaust system for an over-under turbine based combined cycle operating at Mach 0–6. Aerosp Sci Technol. 2019;94(4):105386. doi:10.1016/j.ast.2019.105386.
11. Otobe Y, Kashimura H, Matsuo S, Setoguchi T, Kim H-D. Influence of nozzle geometry on the near-field structure of a highly underexpanded sonic jet. J Fluids Struct. 2008 Feb;24(2):281–93. doi:10.1016/j.jfluidstructs.2007.07.003.
12. Chaudhuri A, Hadjadj A. Numerical investigations of transient nozzle flow separation. Aerosp Sci Technol. 2016 Jun;53:10–21. doi:10.1016/j.ast.2016.03.006.
13. Mo J, Xu J, Gu R, Fan Z. Design of an asymmetric scramjet nozzle with circular to rectangular shape transition. J Propuls Power. 2014 May;30(3):812–9. doi:10.2514/1.B34949.
14. Kumar A, Rathakrishnan E. Experimental investigation of single expansion ramp performance. Proc Inst Mech Eng Part G J Aerosp Eng. 2015 Jun;229(7):1330–5. doi:10.1177/0954410014550051.
15. Lv Z, Xu J, Yu K, Song G. Experimental and numerical investigations of a scramjet nozzle at various operations. Aerosp Sci Technol. 2020 Jan;96(6):105536. doi:10.1016/j.ast.2019.105536.
16. Lv Z, Xu J, Yu K, Song G, Mo J. Experimental and numerical investigations on the mode transition process of an exhaust system for an over-under turbine based combined cycle. Aerosp Sci Technol. 2020 Dec;107(8):106265. doi:10.1016/j.ast.2020.106265.
17. Chen Y, Yu K, Song G, Ge J, Xu J. Design method of scramjet nozzles within predetermined geometrical space and experimental verification. J Aerosp Eng. 2022 Jan;35(1):04021119. doi:10.1061/(ASCE)AS.1943-5525.0001372.
18. Cortes T, Leite V, Ribeiro G, Silva D. Numerical investigation of the flow inside a pilot supersonic combustor test bench. In: Procceeding of the 18th Brazilian Congress of Thermal Sciences and Engineering, 2020. doi:10.26678/ABCM.ENCIT2020.CIT20-0696.
19. Sung B-K, Choi J-Y. Design of a Mach 2 shape transition nozzle for lab-scale direct-connect supersonic combustor. Aerosp Sci Technol. 2021 Oct;117(3):106906. doi:10.1016/j.ast.2021.106906.
20. Hirschen C, Gülhan A, Beck WH, Henne U. Experimental study of a scramjet nozzle flow using the pressure-sensitive-paint method. J Propuls Power. 2008 Jul;24(4):662–72. doi:10.2514/1.34626.
21. Zebbiche T. Supersonic axisymmetric minimum length nozzle conception at high temperature with application for air. J Br Interplanet Soc. 2010 Jan;63:171–91.
22. Sellam M, Zmijanovic V, Leger L, Chpoun A. Assessment of gas thermodynamic characteristics on fluidic thrust vectoring performance: analytical, experimental and numerical study. Int J Heat Fluid Flow. 2015 Jun;53(8):156–66. doi:10.1016/j.ijheatfluidflow.2015.03.005.
23. Chen K, Xu J, Qihao Q, Song G. Three issues on nozzle thrust performance in cold-to-hot correlation considering variable specific heat effect. Phys Fluids. 2022 Jul;34(7):076114. doi:10.1063/5.0098894.
24. Cheng JL, Huang S, Zhou L. Thermal-solid interaction study of serpentine nozzle and analysis on structural response law. J Appl Fluid Mech. 2023 Oct;16(12):2438–58. doi:10.47176/jafm.16.12.2029.
25. Chen Y, Hou Z, Zhu B, Guo Z, Xu B. Validation for aerodynamic performance on over-expanded state of single expansion ramp nozzle configuration. Aerospace. 2022 Nov;9(11):715. doi:10.3390/aerospace9110715.
26. Julian J, Iskandar W, Wahyuni F. Effect of mesh shape and turbulence model on aerodynamic performance at NACA 4415. J Appl Fluid Mech. 2023 Oct;16(12):2504–17. doi:10.47176/jafm.16.12.1983.
27. Yu Y, Yu T, Mao Y, Yang Y, Liang S. Key factors affecting overexpanded flow separation in design of large expansion ratio single expansion ramp nozzle. Aeronaut J. 2024 Sep;5:1–20. doi:10.1017/aer.2024.70.

28. Yu T, Yu Y, Mao YP, Yang YL, Xu SL. Comparative study of OpenFOAM solvers on separation pattern and separation pattern transition in overexpanded single expansion ramp nozzle. J Appl Fluid Mech. 2023 Sep;16(11):2249–62. doi:10.47176/jafm.16.11.1751.
29. Cutler AD, Gallo ECA, Cantu LML, Rockwell RD, Goyne CP. Coherent anti-Stokes Raman spectroscopy of a premixed ethylene-air flame in a dual-mode scramjet. Combust Flame. 2018 Mar;189(1):92–105. doi:10.1016/j.combustflame.2017.10.028.
30. Yu K, Chen Y, Huang S, Xu J. Inverse design method on scramjet nozzles based on maximum thrust theory. Acta Astronaut. 2020 Jan;166:162–71. doi:10.1016/j.actaastro.2019.10.024.